Imaging Heart Motion Using Harmonic Phase MRI

Nael F. Osman, Elliot R. McVeigh, and Jerry L. Prince*

Abstract—This paper describes a new image processing technique for rapid analysis and visualization of tagged cardiac magnetic resonance (MR) images. The method is based on the use of isolated spectral peaks in spatial modulation of magnetization (SPAMM)-tagged magnetic resonance images. We call the calculated angle of the complex image corresponding to one of these peaks a harmonic phase (HARP) image and show that HARP images can be used to synthesize conventional tag lines, reconstruct displacement fields for small motions, and calculate two-dimensional (2-D) strain. The performance of this new approach is demonstrated using both real and simulated tagged MR images. Potential for use of HARP images in fast imaging techniques and three-dimensional (3-D) analyses are discussed.

Index Terms—Image processing, motion estimation, MR tagging, MRI.

I. INTRODUCTION

OVER the last decade, cardiac imaging using tagged magnetic resonance (MR) imaging has become an established technique in medical imaging [1]–[4]. MR tagging uses a special pulse sequence to spatially modulate the longitudinal magnetization of the subject prior to acquiring image data. Over many heartbeats acquired in a single breath hold, enough data can be acquired to reconstruct an image sequence in which the tag pattern is deformed by the underlying motion of the heart [5]. Usually, the tagging process is thought of as producing saturated planes orthogonal to the image plane, leading to images such as that shown in Fig. 1(a). It is not necessary to fully saturate the signal, however, and two-dimensional (2-D) sinusoidal patterns such as that depicted in Fig. 1(b) are also possible. The patterns depicted in Fig. 1(a) and (b) are called spatial modulation of magnetization (SPAMM) tag patterns [6], [7]. This class of patterns forms the basis for the work presented in this paper.

Although significant improvements in the MR tagged image acquisition methodology has occurred [6], [8]–[12], lack of fast quantitative analysis and visualization techniques is preventing MR tagging from being widely adopted in the clinical setting. Most analysis techniques in MR tagging have used image

processing techniques to detect tag features which are then combined into a detailed motion map (displacement and/or strain) using interpolation. To detect tags, for example, Guttman *et al.*[13] used morphological image processing and matched filtering techniques [13], Young and Axel [1] and Kumar and Goldgof [14] used deformable meshes, and Young and Axel have used manually identified points [1]. To interpolate a dense motion, Young and Axel [1] used a finite element model, O'Dell *et al.*[15] used a truncated polynomial expansion, Denney and Prince [16] used a stochastic estimation scheme, and Radeva *et al.*[17] used a three-dimensional (3-D) B-spline.

There are several disadvantages to the existing analysis methods. First, manual intervention is almost always required in feature detection [1], [13]. Although progress is being made in further automating this step (cf. [18]), it is not clear that these methods will ever be completely automatic. Second, because features must by necessity be distinct, interpolation will always be required to achieve dense motion estimation. Third, since the endocardial and epicardial boundaries of the left ventricle are most often explicitly used in the interpolation process, modification to estimate right ventricular motion will require different software and new modeling approaches. Finally, the combined requirements of manual intervention and interpolation makes these methods very time consuming. One cannot hold out great promise that these methods will ever be viable in near real-time diagnosis. The approach described in this paper addresses every one of these concerns.

Optical flow methods have also been explored in the analysis of tagged MR image sequences [19]–[21]. In this approach, sinusoidal tag patterns are used instead of saturated planes. Image brightness gradients become features and together with temporal derivatives estimated from image pairs they can be used to produce dense motion estimates. Generally, regularization is required in order to account for the fact that brightness gradients contain information about motion only in the direction of the gradient. It is possible, however, to combine information from multiple directions, similar in spirit to what is done in planar tagging, in order to produce optical flow estimates without regularization [21]. One limitation of this overall approach is that it is difficult to measure large motions such as that occurring between end diastole and end systole. Instead, successive motions between image frames are measured and tracking is required to measure the total motion [19].

Other techniques exist to measure heart motion using MR without tagging. Velocity encoding techniques use specialized pulse sequences to produce a complex image in which the phase is linearly dependent on the motion [22]. These methods are useful in measuring the flow of body fluids such as blood and cerebrospinal fluids, but cannot measure the large motions present in the heart. Instead, tracking (exactly as in optical
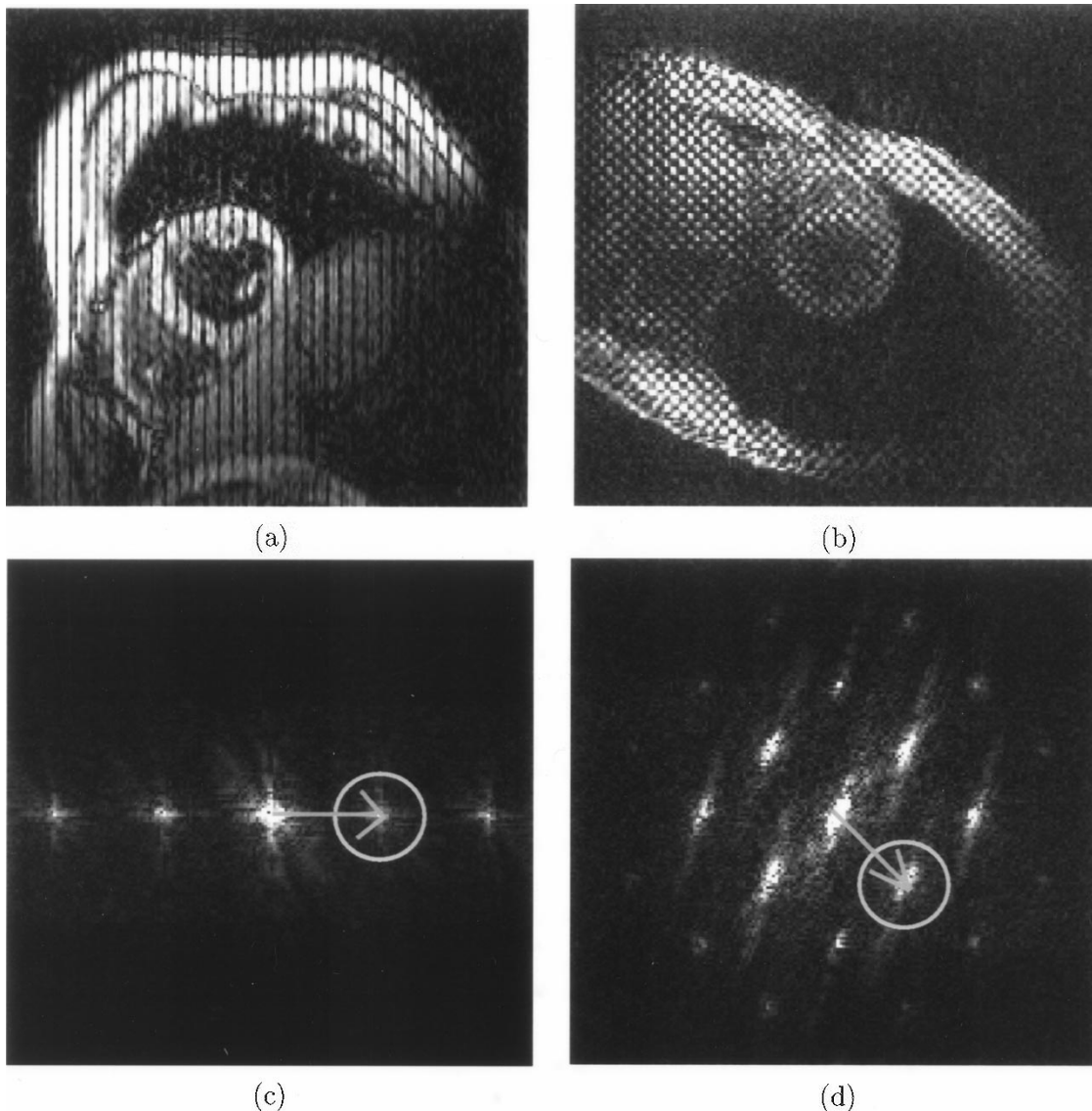
Fig. 1. (a) A 1-D SPAMM-tagged image. (b) A 2-D SPAMM-tagged image. Each shows a short-axis view of the LV of the heart. (c) and (d) are the magnitudes of the Fourier transforms of (a) and (b), respectively. The elongation of the peaks in (d) is orthogonal to the elongated geometry of the cross section of the body in (b).

flow) is required to measure gross motion from successive temporal measurements [23]–[25]. It is also possible to directly measure the temporal derivative of strain, the so-called strain rate [26], [27], but this method is also limited to small motions. Other variations on velocity encoding exist, including the simultaneous use of velocity encoding and tagging [24], [28]. The primary limitations of all the velocity encoding approaches are the inability to measure large motions, low noise immunity, and susceptibility to motion artifacts.

In this paper, we describe a new approach to analyze cardiac tagged MR images using the concept of harmonic phase (HARP) images. The method is based on the fact that SPAMM-tagged MR images [6], [7] have a collection of distinct spectral peaks in the Fourier domain, and that each spectral peak contains information about the motion in a certain direction [11]. The inverse Fourier transform of just one of these peaks, extracted using a bandpass filter, is a complex image whose phase is linearly related to a directional component of the true motion. We define a HARP image to be the principal value of the phase

of this complex image, a number that is constrained to lie in the range $[-\pi, \pi)$ by the wrapping action of the standard inverse arctangent operator. We show in this paper that HARP images can be used to: estimate synthetic tag lines; measure small displacement fields; and compute 2-D strain.

The motion computation methods we describe in this paper use image data corresponding to a single time instant in the cardiac cycle. They do not require a sequence of images as in some other techniques. This distinguishes the methods we describe herein from those in our recent paper describing a technique to track points through images sequences using HARP concepts [29]. The calculations we describe are automatic, fast, and extendable to three dimensions. We show initial experimental results that show promise for fast fully automated imaging of cardiac strain. Several areas for extensions and improvements, including an approach for rapid imaging tuned to the HARP processing methodology, are also described.

The use of local phase information in the estimation of motion from images is not new to HARP. This concept was in fact

developed by several researchers approximately a decade ago [30]–[34] and is now widely known as phase-based optical flow [35], [36]. HARP, however, is different in several respects from the conventional phase-based approaches found in the literature. First, the methods described in this paper are based on the analysis of a single image rather than an image sequence. Thus the concept of velocity-matched, spatio-temporal filters (cf. [37]) cannot be used because an image sequence is not presumed to be available. Second, because of the physical MR tagging process, only two spatial filters are required to unambiguously compute 2-D motion and this motion is related to the true 3-D motion in a known way. These filters are designed according to the expected cardiac strain rather than using velocity-tuned filters as in [32]. Furthermore, Gabor filters are not appropriate in our application because they would unnecessarily attenuate spectral information that should contribute to the motion computations. Finally, in addition to our computation of small displacements, which is similar to the phase-based optical flow methods of Fleet and Jepson [32], HARP uses local phase information to compute local strain. This is an important contribution to the motion-from-phase literature.

II. SPAMM-TAGGED IMAGES

Fig.1(a) and (b) shows two SPAMM-tagged MR images, each showing a short-axis view of a human left ventricle (LV). The spectral peaks appearing in the magnitude of the Fourier transforms of these images, shown in Fig. 1(c) and (d), arise because the tagging process modulates the underlying image with a SPAMM tag pattern. In this section, we develop a mathematical model describing the effect of heart motion on SPAMM-tagged images. In subsequent sections, we present methods to estimate motion from the acquired images.

Our focus throughout this paper is on 2-D MR SPAMM-tagged images because they can be readily acquired on any MR scanner while 3-D image sets are more difficult to prescribe and acquire. Since the heart motion is 3-D, however, we are careful to precisely relate the 2-D quantities we estimate to the true 3-D motion. In this way, the limitations of our methods can be clearly understood and approaches to extend these methods to 3-D imaging can be clearly outlined.

A. SPAMM Tagging

Tagging pulse sequences are usually imposed at end diastole, a time in the cardiac cycle when the left ventricle is full of blood and the heart is relatively slow-moving. The QRS complex of the ECG signals the moment of end diastole. Present technology requires multiple heartbeats, assumed to be perfectly repeating, at least from end diastole to end systole. Under this assumption, the imaging equations governing MR tagging can assume that the entire imaging process takes place in one heart beat. Furthermore, end diastole can be considered to be time $t = 0$ and the position of points within the heart at end diastole can be treated as a material coordinate system, denoted by points $\mathbf{p} \in \mathbb{R}^3$. Let us now consider the effect of the tagging process itself, assumed to take place at $t = 0$ with a stationary heart.

The tagging process imposes a temporary spatial variation in the longitudinal magnetization of the protons inside the body

[7], [8], [38]. SPAMM tag patterns are imposed by applying a sequence of N hard radio frequency (RF) pulses, generally with different tip angles, with T seconds between each pulse. A gradient waveform $\mathbf{G}(t)$ is applied between these pulses and the whole sequence is followed by a crusher to remove the effect of transverse magnetization [7]. The simplest pulse sequence has only two RF pulses and it is called a *1-1 SPAMM* pulse sequence. Now suppose that an image passing through point $\mathbf{p}$ is created immediately after application of the SPAMM tag pulse sequence. Its value is given to good approximation by

$$I(\mathbf{p}) = I_\circ(\mathbf{p}) f(\mathbf{p}; \mathbf{g}) \tag{1}$$

where $I_\circ(\mathbf{p})$ is the value that would have been imaged without tagging and the tag pattern is given by (cf. [39])

$$f(\mathbf{p}; \mathbf{g}) = \sum_{n=0}^{N-1} d_n \cos(n \mathbf{g}^T \mathbf{p}) \tag{2}$$

where d_n are coefficients determined by the sequence of tip angles and the gradient direction $\mathbf{g}$ is given by $\mathbf{g} = \gamma \int_0^T \mathbf{G}(t)\,dt$, where γ is the gyromagnetic ratio. The tag pattern in (2) is one-dimensional (1-D) because its values are identical in planes orthogonal to $\mathbf{g}$. A 2-D SPAMM tag pattern is generated by applying two 1-D SPAMM pulse sequences in rapid succession using two different gradient directions $\mathbf{g}_1$ and $\mathbf{g}_2$. The resulting image value at point $\mathbf{p}$ is

$$I(\mathbf{p}) = I_\circ(\mathbf{p}) f(\mathbf{p}; \mathbf{g}_1) f(\mathbf{p}; \mathbf{g}_2) \tag{3}$$

where it is assumed that the protocols of the two 1-D patterns are identical except for the gradient direction.

Both (1) and (3) describe amplitude modulation of the underlying signal intensity by a pattern of cosines. Because a cosine has two symmetric spectral peaks in Fourier space, a 1-D SPAMM pattern generated with N RF pulses has $2N - 1$ spectral peaks. An example of such a pattern is shown in Fig. 1(a). Because a 2-D SPAMM pattern is the product of two 1-D SPAMM patterns, it has $(2N - 1)^2$ spectral peaks in the Fourier domain. An example of a 2-D SPAMM pattern is shown in Fig. 1(b). The locations $\mathbf{w}_k$ of the spectral peaks in Fourier space are easily found from $\mathbf{g}$ in the 1-D case or $\mathbf{g}_1$ and $\mathbf{g}_2$ in the 2-D case and the resulting tagged image intensity can be written in the following unified manner:

$$I(\mathbf{p}) = \sum_{k=1}^{K} I_\circ(\mathbf{p}) c_k e^{j \mathbf{w}_k^T \mathbf{p}} \tag{4}$$

where $K = (2N - 1)$ for 1-D SPAMM and $K = (2N - 1)^2$ for 2-D SPAMM. The coefficients c_k are readily determined from d_k.

B. Motion and Images

In order to relate calculations made using 2-D tagged images to the actual 3-D motion, it is necessary to establish a mathematical relationship between the motion of the heart, the physical position of pixels within an image, and the intensities of tagged images.

As the heart deforms, a material point within the myocardium moves from its reference position $\mathbf{p}$ to a new spatial position $\mathbf{x}$ at time t. The reference map $\mathbf{p}(\mathbf{x}, t)$ characterizes this motion by giving the material position $\mathbf{p}$ of the spatial point $\mathbf{x}$ at time t. Using $\mathbf{p}(\mathbf{x}, t)$ in place of $\mathbf{p}$ in (4) gives a relationship involving the spatial coordinate $\mathbf{x}$ instead of the material coordinate $\mathbf{p}$.

Now suppose the location of a pixel within an image is designated by the 2-D image coordinate vector $\mathbf{y} = [y_1 \ y_2]^T$. Then the 3-D position $\mathbf{x}$ of the pixel at image coordinate $\mathbf{y}$ can be described by the function $\mathbf{x}(\mathbf{y}) = y_1 \mathbf{h}_1 + y_2 \mathbf{h}_2 + \mathbf{x}_0$ where $\mathbf{h}_1$ and $\mathbf{h}_2$ are two 3-D orthogonal unit vectors describing the image orientation and $\mathbf{x}_0$ is an image origin. This function can be written in matrix notion as follows:

$$\mathbf{x}(\mathbf{y}) = H\mathbf{y} + \mathbf{x}_0 \qquad (5)$$

where $H = [\mathbf{h}_1 \ \mathbf{h}_2]$. Using $\mathbf{x}(\mathbf{y})$ in $\mathbf{p}(\mathbf{x}, t)$ and substituting $\mathbf{p}(\mathbf{x}, t)$ for $\mathbf{p}$ in (4) yields the following expression for a SPAMM-tagged MR image:

$$I(\mathbf{y}, t) = \sum_{k=1}^{K} I_k(\mathbf{y}, t) \qquad (6)$$

where

$$I_k(\mathbf{y}, t) = I_\circ(\mathbf{p}(\mathbf{x}(\mathbf{y}), t)) c_k(t) e^{j\mathbf{w}_k^T \mathbf{p}(\mathbf{x}(\mathbf{y}), t)}. \qquad (7)$$

Here, the coefficients c_k are made functions of time to account for the fading of tag patterns caused by longitudinal relaxation and the imaging pulse sequence. Equation (6) shows that a SPAMM-tagged image is the sum of K complex images, which we call *harmonic images*, each corresponding to a distinct spectral peak identified by the frequency vector $\mathbf{w}_k$.

In the following development we implicitly assume that all gradient directions $\mathbf{g}$ are oriented parallel to the image plane. That is, they are linear combinations of $\mathbf{h}_1$ and $\mathbf{h}_2$. This implies that $\mathbf{w}_k, k = 1, \ldots, K$ are also parallel to the image plane. This is the tagging protocol most commonly implemented in practice and is best for imaging the desired 2-D motion quantities from a single image plane. The consequences of using $\mathbf{g}$ pointing out of the plane (cf. [40]) are interesting since there is the potential to directly estimate certain 3-D motion quantities but such a development is beyond the scope of the present paper.

III. HARMONIC PHASE IMAGES

A. Displacement Modulation

Interpretation of the action of motion as a modulation process is key to the methods developed herein (see also [41], [42]). We can see this relationship by examining the kth harmonic image $I_k(\mathbf{y}, t)$ that corresponds to the kth spectral peak in the Fourier transform of $I(\mathbf{y}, t)$. One important description of motion is the displacement field, defined as

$$\mathbf{u}(\mathbf{x}, t) = \mathbf{x} - \mathbf{p}(\mathbf{x}, t). \qquad (8)$$

Using this expression in (7) yields

$$I_k(\mathbf{y}, t) = D_k(\mathbf{y}, t) e^{j\mathbf{w}_k^T \mathbf{x}(\mathbf{y})} e^{-j\mathbf{w}_k^T \mathbf{u}(\mathbf{x}(\mathbf{y}), t)} \qquad (9)$$

where $D_k(\mathbf{y}, t) = I_\circ(\mathbf{p}(\mathbf{x}(\mathbf{y}), t)) c_k(t)$. Replacing $\mathbf{x}(\mathbf{y})$ by the expression in (5) and expanding yields

$$I_k(\mathbf{y}, t) = D_k(\mathbf{y}, t) e^{j\left[(H^T \mathbf{w}_k)^T \mathbf{y} + \mathbf{w}_k^T \mathbf{x}_0\right]} e^{-j\mathbf{w}_k^T \mathbf{u}(\mathbf{x}(\mathbf{y}), t)}$$
$$(10)$$

The first exponential term in (10) represents a simple complex sinusoidal carrier with frequency $H^T \mathbf{w}_k$ and phase $\mathbf{w}_k^T \mathbf{x}_0$. This carrier determines the position of the spectral peak at $H^T \mathbf{w}_k$ in the Fourier domain. The term $D_k(\mathbf{y}, t)$ multiplies this complex sinusoid, so it represents amplitude modulation (AM) in analogy with communications theory. Using the same analogy, the last term in (10) is the most interesting term, as it represents a phase modulation (PM) of the underlying carrier by the displacement field $\mathbf{u}$. This property is what we exploit in our development of motion estimation methods. To complete the analogy with communications theory, it has been in shown in [41] that the gradient of the phase, which we called the local spatial frequency is modulated by the local strain. This is analogous to frequency modulation (FM) in communications theory.

Although the spectrum of I_k is spread throughout the Fourier domain, most of its energy is concentrated, due to the nature of the LV motion, around the spectral peak located at $H^T \mathbf{w}_k$. The extent of the energy localization is affected by the motion, which in the case of contracting heart is manifested by the spreading of the spectral peaks. It is worth mentioning that a rigid rotation of the pattern would change the angular position of the spectral peaks. Fortunately, the heart's twisting during systole causes only a small angular motion of the spectral peaks. It is possible to extract an estimate of the harmonic image using a 2-D bandpass filter centered around $H^T \mathbf{w}_k$ whose size is large enough to capture the spectral peak after maximum spreading. This estimate will differ from the truth because of both sampling and noise effects and also because of both energy lost outside of the bandpass region and energy entering the bandpass region from other spectral peaks. Designing an appropriate bandpass filter is largely a matter of trading off the loss of accuracy when the bandpass region is too small with the introduction of artifacts when the bandpass region is too big. We give an empirical study for optimizing these filters in Section I-C. For now, we assume that a bandpass filter is capable of extracting I_k exactly.

B. HARP Images

Since the harmonic image $I_k(\mathbf{y}, t)$ is complex, it has both a magnitude and phase at each $\mathbf{y}$. From (7) we see that the phase of I_k is an image given by

$$\phi_k(\mathbf{y}, t) = \mathbf{w}_k^T \mathbf{p}(\mathbf{x}(\mathbf{y}), t). \qquad (11)$$

which we refer to as a *harmonic phase image*. We define a *HARP image* to be the calculated phase of I_k, which is given by

$$a_k(\mathbf{y}, t) = \angle I_k(\mathbf{y}, t), \quad 1 \le k \le K \qquad (12)$$

where

$$\angle I_k = \begin{cases} \tan^{-1} \dfrac{\text{Im}\{I_k\}}{\text{Re}\{I_k\}}, & \text{Re}\{I_k\} \ge 0 \\[2ex] \pi + \tan^{-1} \dfrac{\text{Im}\{I_k\}}{\text{Re}\{I_k\}}, & \text{otherwise.} \end{cases} \qquad (13)$$
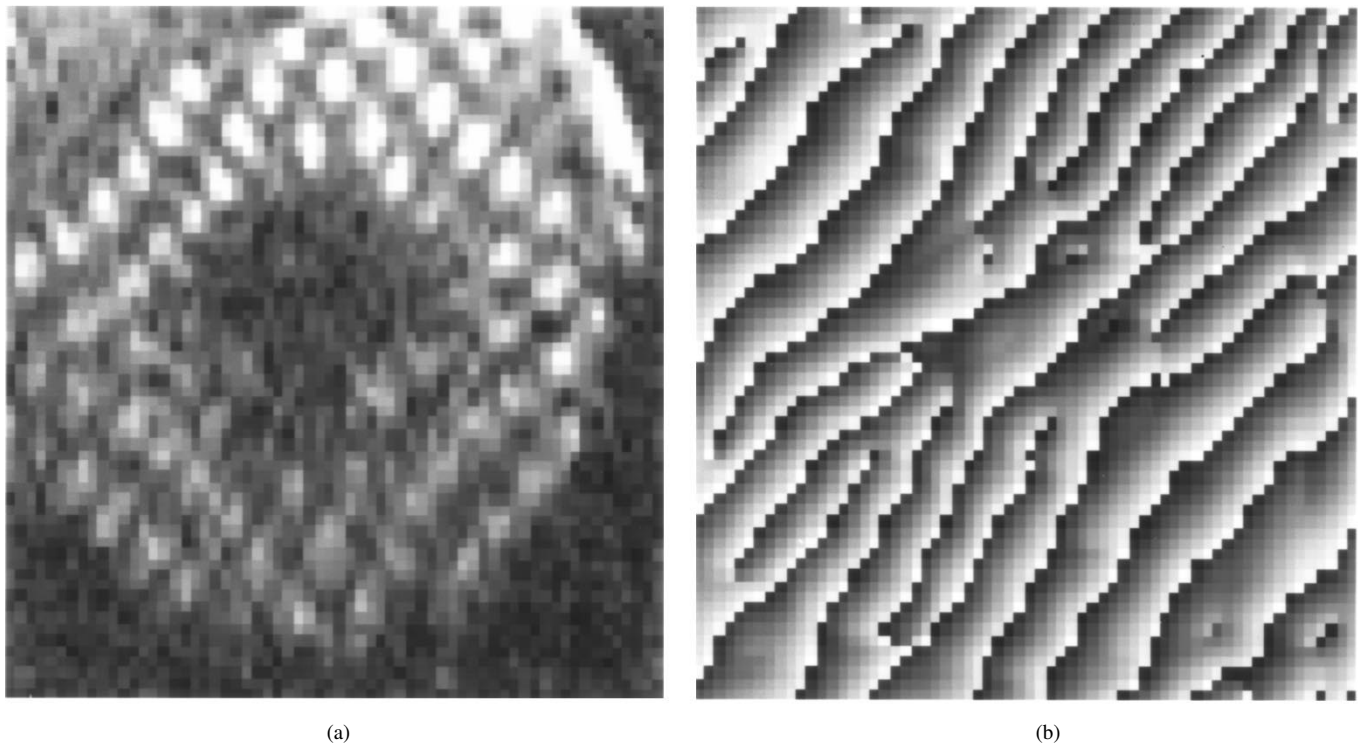
| (a) | (b) |

Fig. 2. (a) 2-D 1-1 SPAMM-tagged short axis image of the left ventricle and (b) one of its angle images. Notice that the branching and truncation in (b) occurs outside the myocardium in regions where the underlying image intensity in (a) is very small and noise dominates.

Because of the inverse tangent operator, a HARP image is the principal value of its corresponding phase image, and is restricted to be in the range $[-\pi, +\pi)$. Formally, a HARP image is related to the phase image as follows:

$$a_k(\mathbf{y}, t) = \mathcal{W}(\phi_k(\mathbf{y}, t)) \qquad (14)$$

where the nonlinear wrapping function is given by

$$\mathcal{W}(\phi) = \mod(\phi + \pi, 2\pi) - \pi. \qquad (15)$$

From (11), we see that ϕ_k is linearly related to the reference map $\mathbf{p}$, so it could be used in a fairly straightforward manner to calculate motion and motion-related quantities. Unless ϕ_k happens to fall into the range $[-\pi, +\pi)$, however, to actually calculate ϕ_k requires the use of 2-D phase unwrapping techniques [43], which are very sensitive to noise. Although robust least squares techniques have been developed [44]–[46], these algorithms are fairly time-consuming and do not always work properly [46]. We can expect this process to be particularly problematic in the high-noise environment of cardiac tagged MR imaging. Instead, the motion estimation procedures described in this paper rely only on having the HARP images, which are readily computed in a very robust manner using (13). It should be noted that both the phase and the HARP angle are material properties of the tagged tissue, so that if one follows a particular material point $\mathbf{p}$, its phase and HARP angle remain constant with time. This is an important property, which will be exploited in Section III-C, where we describe the use of HARP images in measuring motion.

As a demonstration, we calculated HARP images for the image sequence whose first image appears in Fig. 1(b) using the spectral peak circled in Fig. 1(d). A close-up image of the

LV near end systole is shown in Fig. 2(a) and its HARP image is shown in Fig. 2(b). The strongest apparent features in this HARP image are the lines of discontinuity traveling at a $45°$ angle. These lines correspond to the transition in angle from $+\pi$ to $-\pi$ caused by the wrapping in (15). Since these lines correspond well to the apparent movement of the tag pattern itself, they demonstrate the fact that the tag pattern phase is a material tissue property, remaining constant despite fading and intensity variations of the tag pattern itself.

C. Measuring Motion Using HARP Images

We now outline three ways to use HARP images in cardiac motion analysis from tagged MR images. Experiments showing their use and performance are given in Section IV.

1) Synthetic Tag Lines: The discontinuities in Fig. 2(b) strongly resemble 1-D tag lines. In fact, the lines we see in this figure represent a crude (pixelated) approximation of image isocontours having the value π. Since the HARP angle of a tagged image is a material property of the tissue, these lines represent samples of surfaces all having the angle π. These surfaces are completely analogous to tag surfaces arising from planar tagging or higher-order 1-D SPAMM tagging and the lines are analogous to the intersection of image planes with these tag surfaces. In essence, HARP images can be used to generate synthetic tag lines by identifying isocontours within the HARP images.

Mathematically, a set of tag lines $\mathcal{L}_k(a)$ is defined by

$$\mathcal{L}_k(a) = \{\mathbf{y} \,|\, a_k(\mathbf{y}, t) = a\} \qquad (16)$$

where $a \in [-\pi, \pi)$ is an arbitrary angle. Computationally, $\mathcal{L}_k(a)$ is determined by running an isocontour algorithm at

level a on image $a_k(\mathbf{y}, t)$. After restricting these lines to those falling within the LV myocardium, they can then be used in any standard analysis procedure based on planar tags (cf. [6], [15]).

There are several advantages in using HARP images to generate synthetic tag lines. First, it is a completely automatic process. Second, the tag lines will have subpixel resolution since good isocontour algorithms have this property (see results in Section IV). Third, the entire image will have these tags automatically identified, including those passing through both left and right ventricular myocardium. Finally, tags spaced very closely together can be generated by selecting N values in the range $[-\pi, \pi]$ so that N tag lines will be synthesized within over the spatial period $2\pi / \|H^T \mathbf{w}_k\|$. In principle, there is no fundamental limit on how close these tag lines can be spaced, because they are not limited by the detectability of features spaced close together.

2) Measuring Small Motions: Consider the point $\mathbf{y}$ in the image plane at time t. The position of this material point at $t = 0$ is given by the reference map $\mathbf{p}(\mathbf{x}(\mathbf{y}), t)$, which is a point not usually in the image plane. Now suppose we measure two harmonic images of the form (10) having linearly-independent tag frequencies $\mathbf{w}_k$ and $\mathbf{w}_l$ parallel to the image plane. Since the phases ϕ_k and ϕ_l of the harmonic images are material properties, the point $\mathbf{p}(\mathbf{x}(\mathbf{y}), t)$ has the same phases as does $\mathbf{y}$ at t. Furthermore, since $\mathbf{w}_k$ and $\mathbf{w}_l$ are parallel to the image plane, the orthogonal projection of $\mathbf{p}(\mathbf{x}(\mathbf{y}), t)$ onto the image plane also has these same phases. Although the true motion of any point in the heart is 3-D, the apparent motion in 2-D is uniquely defined between the projection of the point $\mathbf{p}(\mathbf{x}(\mathbf{y}), t)$ on the image plane and its spatial position $\mathbf{y}$. For small motions (to be defined precisely below), we can directly measure the apparent motion.

Given the complete knowledge of the tagging pulse sequence and given the measured HARP image $a_k(\mathbf{y}, t)$, the following quantity can be calculated:

$$\Delta a_k(\mathbf{y}, t) = \mathcal{W}\left[\mathbf{w}_k^T \mathbf{x}(\mathbf{y}) - a_k(\mathbf{y}, t)\right]. \qquad (17)$$

The 3-D displacement can be written as $\mathbf{u} = u_1 \mathbf{h}_1 + u_2 \mathbf{h}_2 + u_3 \mathbf{h}_3$ where $\mathbf{h}_3 = \mathbf{h}_1 \times \mathbf{h}_2$. It is shown in Appendix A that, provided that $\mathbf{w}_k$ and $\mathbf{w}_l$ are linearly independent and $|\mathbf{w}_i^T \mathbf{u}| < \pi$, $i = k, l$, the 2-D displacement within the image plane $\mathbf{u}_2 = [u_1 \ u_2]$ can be calculated according to

$$\mathbf{u}_2(\mathbf{y}, t) = (W^T H)^{-1} \begin{bmatrix} \Delta a_k(\mathbf{y}, t) \\ \Delta a_l(\mathbf{y}, t) \end{bmatrix} \qquad (18)$$

where $W = [\mathbf{w}_k \ \mathbf{w}_l]$. This is our estimate of 2-D displacement for small motions.

There are several ways to assure that the conditions $|\mathbf{w}_i^T \mathbf{u}| < \pi$, $i = k, l$ are satisfied to make (18) valid. First, it is possible to image very shortly after end diastole, before there is substantial heart motion. This will be useful, and potentially clinically important in the first few tens of milliseconds of systole, but will not allow the calculation of displacements throughout the systolic phase. Second, if low-frequency tag patterns are used, the physical period of the tag pattern is larger, so larger motions will not produce angle ambiguity (wrapping). The difficulty here is that the spectral peaks of low-frequency patterns

will often interfere with one another, leading to motion artifacts. A third possibility is to apply the tag pattern at a fixed offset from end diastole and image shortly thereafter.

We note that (18) is a direct consequence of having two linearly independent brightness constraint equations arising from the HARP images a_k and a_l. This equation represents a special case of the phased-based optical flow method proposed by Jepson and Fleet [32]. Here, however, only two filters are sufficient to reconstruct an arbitrary 2-D displacement field because there is sufficient energy and isolation in the spectral peaks arising from the MR tagging process. The following section presents an approach to the measurement of local strain, representing a significant extension to the past literature on the use of local phase information. In particular, strain is estimated using only a pair of HARP images acquired at any time during the cardiac cycle (provided that the tags persist). The fact that no reference images are required and that the calculation is exact despite large deformations is important to the practice of cardiac strain imaging.

3) Measuring Strain: Assume we have measured two HARP images having linearly independent frequencies $\mathbf{w}_k$ and $\mathbf{w}_l$ parallel to the plane. Let $\mathbf{q}(\mathbf{y}, t) \equiv \mathbf{y} - \mathbf{u}_2(\mathbf{y}, t)$ be the 2-D reference map describing the point in the image plane having the same two phases at time $t = 0$ as does the point $\mathbf{y}$ at time t. Now let $\mathbf{e} \in \mathbb{R}^2$ be a unit vector in the image plane. The apparent strain in the direction $\mathbf{e}$ is given by

$$\epsilon_2(\mathbf{y}, t; \mathbf{e}) = \|[\nabla_{\mathbf{y}} \mathbf{q}(\mathbf{y}, t)]^{-1} \mathbf{e}\| - 1 \qquad (19)$$

where $\nabla_{\mathbf{y}} \mathbf{q}$ is the tensor corresponding to the derivative of $\mathbf{q}$ with respect to $\mathbf{y}$, represented in matrix form by $[\partial q_m / \partial y_n]$, $m, n = 1, 2$. One possible way to calculate this quantity would be to first calculate $\mathbf{u}_2$ using (18), which determines $\mathbf{q}(\mathbf{y}, t)$, and then use (19). This calculation would be limited to small motions, however, and, as we now show, it is possible to calculate ϵ_2 without this limitation.

It is shown in Appendix B that

$$\nabla_{\mathbf{y}} \mathbf{q}(\mathbf{y}, t) = (W^T H)^{-1} \nabla_{\mathbf{y}} \phi(\mathbf{y}, t) \qquad (20)$$

where $\phi = [\phi_k \ \phi_l]^T$. From (14), we see that the gradient of a HARP image is the same as the gradient of a phase image except at the points of discontinuity caused by the wrapping operation. At these points, the gradient is theoretically infinite and practically very large. It is possible to shift the locations of the wrapping artifact, however, by simply adding π to the HARP image and rewrapping. Gradients calculated at locations of the previous discontinuities are now equal to the gradient of the phase image at that location. Therefore

$$\nabla_{\mathbf{y}} \phi_i = \nabla_{\mathbf{y}}^* a_i \qquad (21)$$

for $i = k, l$ where the modified gradient operator $\nabla_{\mathbf{y}}^*$ is defined by

$$\nabla_{\mathbf{y}}^* a_i = \begin{cases} \nabla_{\mathbf{y}} a_i, & \|\nabla_{\mathbf{y}} a_i\| \leq \|\nabla_{\mathbf{y}} \mathcal{W}(a_i + \pi)\| \\ \nabla_{\mathbf{y}} \mathcal{W}(a_i + \pi), & \text{otherwise}. \end{cases} \qquad (22)$$

Now, using (21) in (20) yields

$$\nabla_{\mathbf{y}} \mathbf{q}(\mathbf{y}, t) = (W^T H)^{-1} \nabla_{\mathbf{y}}^* \mathbf{a}(\mathbf{y}, t) \qquad (23)$$
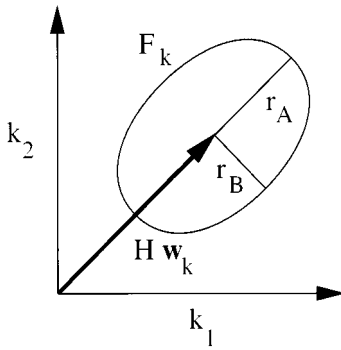
Fig. 3. The elliptical passband of filter F_k.

where $\mathbf{a} = [a_k \ a_l]^T$. Substituting (23) into (19) yields

$$\epsilon_2(\mathbf{y}, t; \mathbf{e}) = \|[\nabla_{\mathbf{y}}^* \mathbf{a}(\mathbf{y}, t)]^{-1} W^T H \mathbf{e}\| - 1 \qquad (24)$$

which is our estimate of apparent strain in a 2-D image plane. It can always be computed provided that $\mathbf{w}_k$ and $\mathbf{w}_l$ are linearly independent, in particular, it is not limited by the small motion assumption.

IV. EXPERIMENTAL RESULTS

In this section, we present experimental results related to the acquisition of and uses for HARP images. The first set of experiments is designed to determine the best position, size, and shape of the bandpass filters required to compute HARP images from acquired SPAMM-tagged MR images. The second set of experiments is designed to demonstrate and quantify the performance of the three applications of HARP images to motion estimation.

A. Computing HARP Images

1) Bandpass Filter: The first step in computing a HARP image is to acquire its harmonic image $I_k(\mathbf{y}, t)$, which can be estimated by applying a bandpass filter to the image $I(\mathbf{y}, t)$. The true Fourier spectrum of the harmonic image I_k is determined by the frequency $\mathbf{w}_k$, the spectrum of the underlying image, and the motion. Since its spectrum is strongly peaked around $H^T \mathbf{w}_k$ (see Section III-A), we positioned the bandpass region of the filter at $H^T \mathbf{w}_k$, as shown in Fig. 3. We chose an ellipse for the shape of the bandpass region because it has a simple geometry that adequately captures the gross shape of most spectral peaks. We fixed the major axis of the ellipse to be in the direction of $H^T \mathbf{w}_k$ because we expect that most of the spectral changes due to motion will be in this direction.

Letting $\mathbf{k} \in \mathbb{R}^2$ denote 2-D frequency, the bandpass filter we used is given in the Fourier domain by

$$F_k(\mathbf{k}) = \begin{cases} 1, & s_k(\mathbf{k}) \le 1 \\ e^{-(s_k(\mathbf{k})-1)^2/(2\sigma^2)}, & s_k(\mathbf{k}) > 1 \end{cases} \qquad (25)$$

where

$$s_k(\mathbf{k}) = \|(R_k S)^{-1}(\mathbf{k} - H^T \mathbf{w}_k)\|. \qquad (26)$$

Here, $S = \text{diag}[r_A, r_B]$, where r_A and r_B are the major and minor radii of the elliptic bandpass region in units of rad/cm; R is an Euler matrix corresponding to a rotation by $\angle H^T \mathbf{w}_k$; and $\sigma = 0.05$ (unitless) in all our experiments. The function $s_k(\mathbf{k})$

yields the desired position, size, and shape of the main elliptical bandpass region. The actual filter $F_k(\mathbf{k})$ is unity within this region, but to reduce ringing artifacts it tails off in a Gaussian fashion outside this region.

Given the described bandpass filter, the harmonic image is estimated using $\hat{I}_k(\mathbf{y}, t) = \mathcal{F}^{-1}\{F_k \cdot \mathcal{F}\{I(\mathbf{y}, t)\}\}$ where the operators $\mathcal{F}$ and $\mathcal{F}^{-1}$ represent the Fourier transform and its inverse, respectively. The corresponding HARP image is then estimated as $\hat{a}_k(\mathbf{y}, t) = \angle \hat{I}_k(\mathbf{y}, t)$ (Section III-B). The radii of the ellipse, r_A and r_B, should be selected to minimize the error in this estimate, since this affects all other estimated motion quantities. We now describe how to characterize this error.

Suppose it was possible to estimate the phases $\hat{\phi}_k$ and $\hat{\phi}_l$ from two estimated harmonic images (for example by phase unwrapping their corresponding HARP images). Then 2-D reference map could be estimated as follows [see (32)]:

$$\hat{\mathbf{q}}(\mathbf{y}, t) = (W^T H)^{-1}[\hat{\phi}(\mathbf{y}, t) - W^T \mathbf{x}_0] \qquad (27)$$

where $\hat{\phi} = [\hat{\phi}_k \ \hat{\phi}_l]^T$. Using (32) and (27), the error in this estimate can be written as

$$\tilde{\mathbf{q}} = \mathbf{q} - \hat{\mathbf{q}} = (W^T H)^{-1}[\phi - \hat{\phi}]. \qquad (28)$$

If the error were small, i.e., $|\phi - \hat{\phi}| < \pi$—then $\phi - \hat{\phi} = \mathbf{a} - \hat{\mathbf{a}}$ and

$$\tilde{\mathbf{q}} = (W^T H)^{-1}[\mathbf{a} - \hat{\mathbf{a}}] \qquad (29)$$

In the simulation experiments described below, the error was small enough to use (29). Moreover, in the simulation, we know the true reference map $\mathbf{p}$ and we can compute $\mathbf{a}(\mathbf{y}, t)$ using (11) and (14). Therefore, the error as $\|\tilde{\mathbf{q}}(\mathbf{y}, t)\|$ can be computed at each point in the image.

2) Parameter Optimization: Quantitative experiments designed to optimize the selection of r_A and r_B for a given tag frequency were conducted. We used images generated by a simulation program designed in our laboratory, an early version of which was reported in [47]. The program simulates the normal deformation of the LV during systole and produces realistic tagged MR images. The smooth motion field produced by this simulation might not capture some of the more abrupt motion patterns of normal myocardium, but should apply in the case of diseased myocardium since it is less active.

A typical image generated from our simulator is shown in Fig. 4(a), which can be compared to an actual image shown in Fig. 2(a). The image in Fig. 4(a) was simulated using a 2-D SPAMM tag pattern. The gradients between the RF pulses produces a 6-mm tag period in the two diagonal directions. For each direction, the SPAMM pulse sequence has two RF pulses with a $45°$ tip angle each. The simulated image represents an end-systolic image, so it includes the effect of motion, producing the maximum spreading of the spectral peaks, and tag fading assuming myocardial tissue parameters of $T_1 = 900$ ms and $T_2 = 100$ ms. The image matrix size is 64×64 with a 1.09-mm pixel separation. The nine spectral peaks present in this 2-D 1-1 SPAMM pattern are evident in the magnitude of the Fourier transform of this image, as shown in Fig. 4(b). Seven similar short-axis images were produced simulating the appearance of the LV at end systole given fundamental 1-1 2-D SPAMM tag
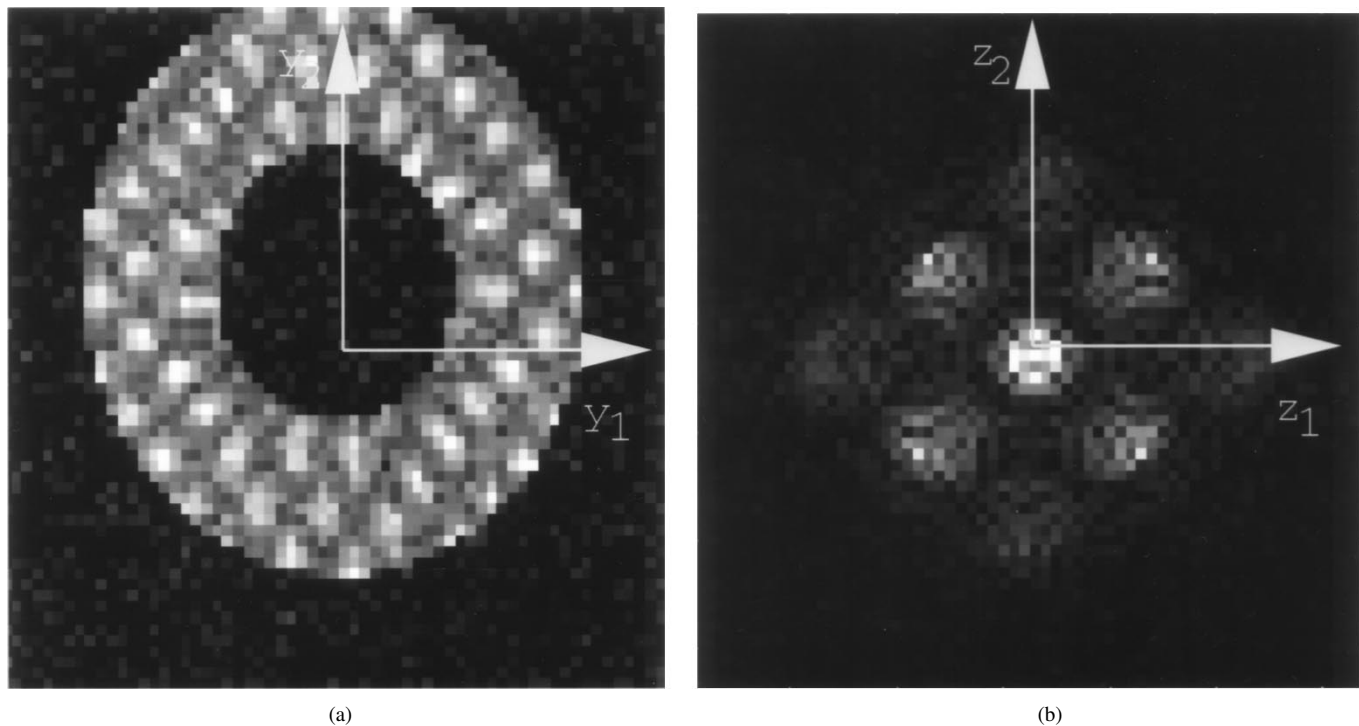
Fig. 4. (a) A simulated 2-D 1-1 SPAMM-tagged image with a 6-mm tag period. (b) The magnitude of its Fourier transform.

periods of 2, 3, 4, 5, 6, 7, and 8 mm. We also obtained the true 3-D reference map, so we could calculate the root-mean-square (rms) displacement error over the simulated myocardium.

Two bandpass filters F_k and F_l were used to estimate the HARP images a_k and a_l. The center frequencies of these filters were given by

$$H^T \mathbf{w}_k = \frac{2\pi}{S_P} \begin{bmatrix} \frac{1}{\sqrt{2}} \\ \frac{1}{\sqrt{2}} \end{bmatrix} \quad \text{and} \quad H^T \mathbf{w}_l = \frac{2\pi}{S_P} \begin{bmatrix} \frac{-1}{\sqrt{2}} \\ \frac{1}{\sqrt{2}} \end{bmatrix}$$

where S_P is the tag period. To determine the best radii for the filters, the rms error $\tilde{\mathbf{q}}$ was computed for different values of the radii r_A and r_B. Those radii yielding the lowest rms error for each tag period, the optimal radii, are plotted in Fig. 5(a). There are two reasons why the optimal radii increase with increasing tag frequency. First, it can be shown theoretically that the amount of frequency spreading caused by the phase modulation effect of motion increases with increasing tag frequency. This is a standard result in communications theory. Second, as the spectral peaks get farther away from the origin, there is less interference with the spectral peak at dc. The optimal radii plotted in Fig. 5(a) were used in all subsequent experiments in this section for both real and simulated data.

Fig. 5(a) also shows the rms error of the optimal radii plotted as a function of the tag period. We observe that the error generally decreases with increasing tag frequency. There are two reasons for this. First, there is less overlap with the dc spectral peak as frequency increases, reducing the associated artifacts. Second, the larger number of pixels within the larger bandpass region at the higher frequencies gives more information about the modulated motion spectrum. Finally, the reason that the error increases at tag period 2 mm is that high-frequency

parts of the two spectral peaks were truncated in the Fourier domain, i.e., the highest frequencies were not imaged. To study the effect of image noise, we added different levels of white Gaussian noise to the simulated images and computed the rms displacement errors. These results are summarized in Fig. 5(b), where the rms displacement error is plotted against the noise ratio for four tag periods. The noise ratio is defined as the ratio of the noise standard deviation to the maximum image magnitude (the reciprocal of the SNR is used so that we can plot the zero-noise case). As is typical in FM and PM communications systems, we see that the performance degrades gradually as the noise increases.

B. Magnitude and HARP Images

1) Magnitude Images: So far, we have concentrated entirely on the angle of the harmonic image I_k because it contains information about cardiac motion. The magnitude (modulus) of I_k is also useful, however, because it contains information about cardiac geometry. Consider the horizontal and vertical planar tagged image sequences shown in Fig. 6. These images have 64×64 pixels with 1.25-mm pixel separation, cropped from the original images to show close-up short-axis images of the deforming LV during systole. The first image in each sequence corresponds to 47.3 ms after end diastole and subsequent images are 32.5-ms apart. Using the spectral peaks corresponding to the first harmonic of each image, we used the optimal bandpass filters to compute two sequences of harmonic images. Then, for each time frame, we computed the average of the magnitudes of the two harmonic images produced from the two tag orientation images. An image sequence showing the average magnitude image is shown in Fig. 7(a). The quality of these images is quite low because we are using only a very small part of Fourier space to reconstruct the geometry.
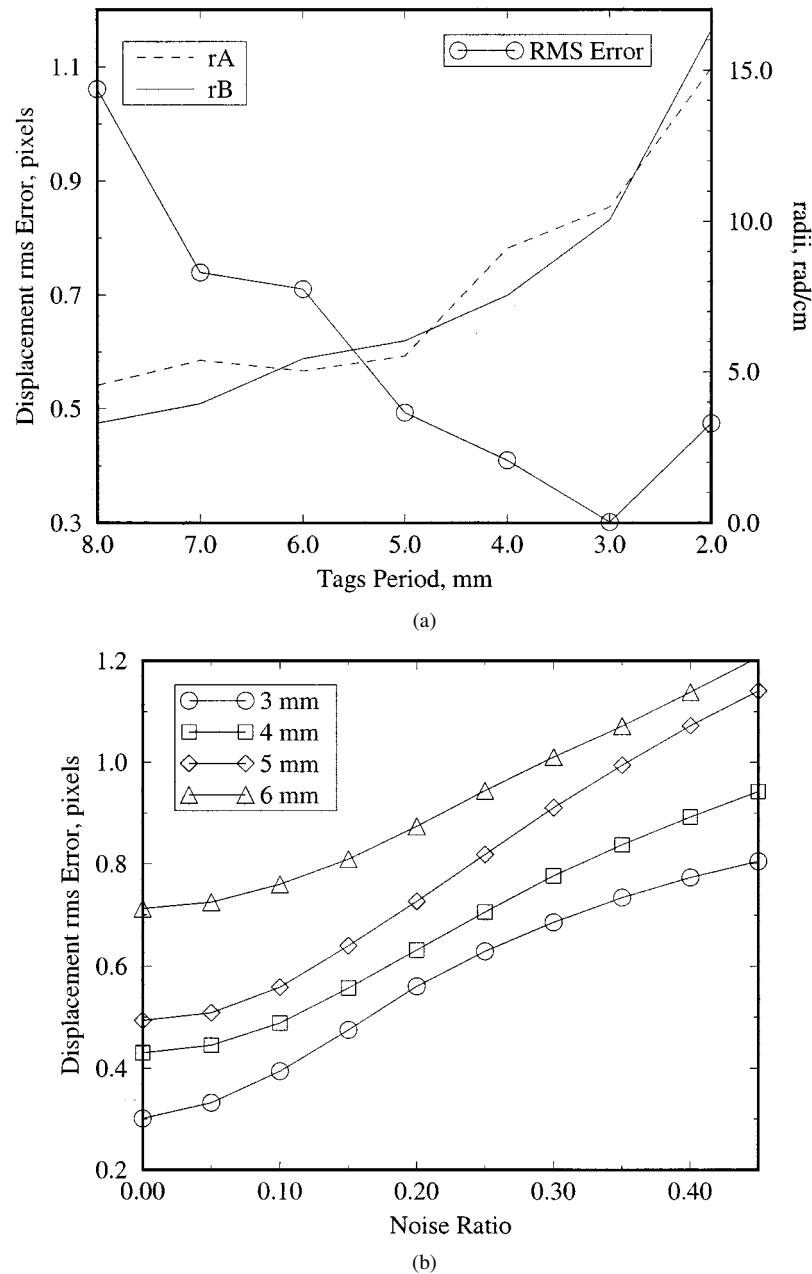
(a)

(b)

Fig. 5.   (a) Optimal radii of the elliptical bandpass filter as a function of tag period: rms displacement error as a function of tag period. (b) RMS displacement error versus noise fraction for different tag periods.

As tags fade, the energy of the signal in the neighborhood of a spectral peaks diminishes. Since there is no dc component in a bandpass filter, the reduction in intensity evident in the image sequence of Fig. 7(a) reflects this tag fading. The calculated energy in a harmonic image can, in fact, be used to compensate for the effects of tag fading by simply multiplying each image so that it has the same energy as the first image. Applying this simple correction scheme to the images in Fig. 7(a) yields the corresponding normalized images in Fig. 7(b). Although far from ideal representations of the myocardial geometry, these images can be used in fast segmentation for visualization of computed motion quantities within the myocardium.

2) Examples of HARP Images: HARP images computed using the first harmonic of the images in Fig. 6 are shown in Fig. 8. For display purposes, they are shown overlaid on a simple threshold segmentation of the normalized magnitude images in Fig. 7(b). While it is somewhat misleading to look at the very jagged-looking HARP images themselves, a certain key point can be made. We observe that the bending of the saw-tooth pattern in the HARP images is similar to the bending of the tag lines in the original images. This reflects the fact that the HARP angle is a material property of the tissue that follows the motion of the LV.

C. Motion Estimation Experiments

1) Synthetic Tag Lines: Fig. 9 shows three examples of synthetic tag generation. In all three cases, the synthetic tags were created using an isocontour algorithm, and the resulting lines were manually trimmed to remove lines outside of the region
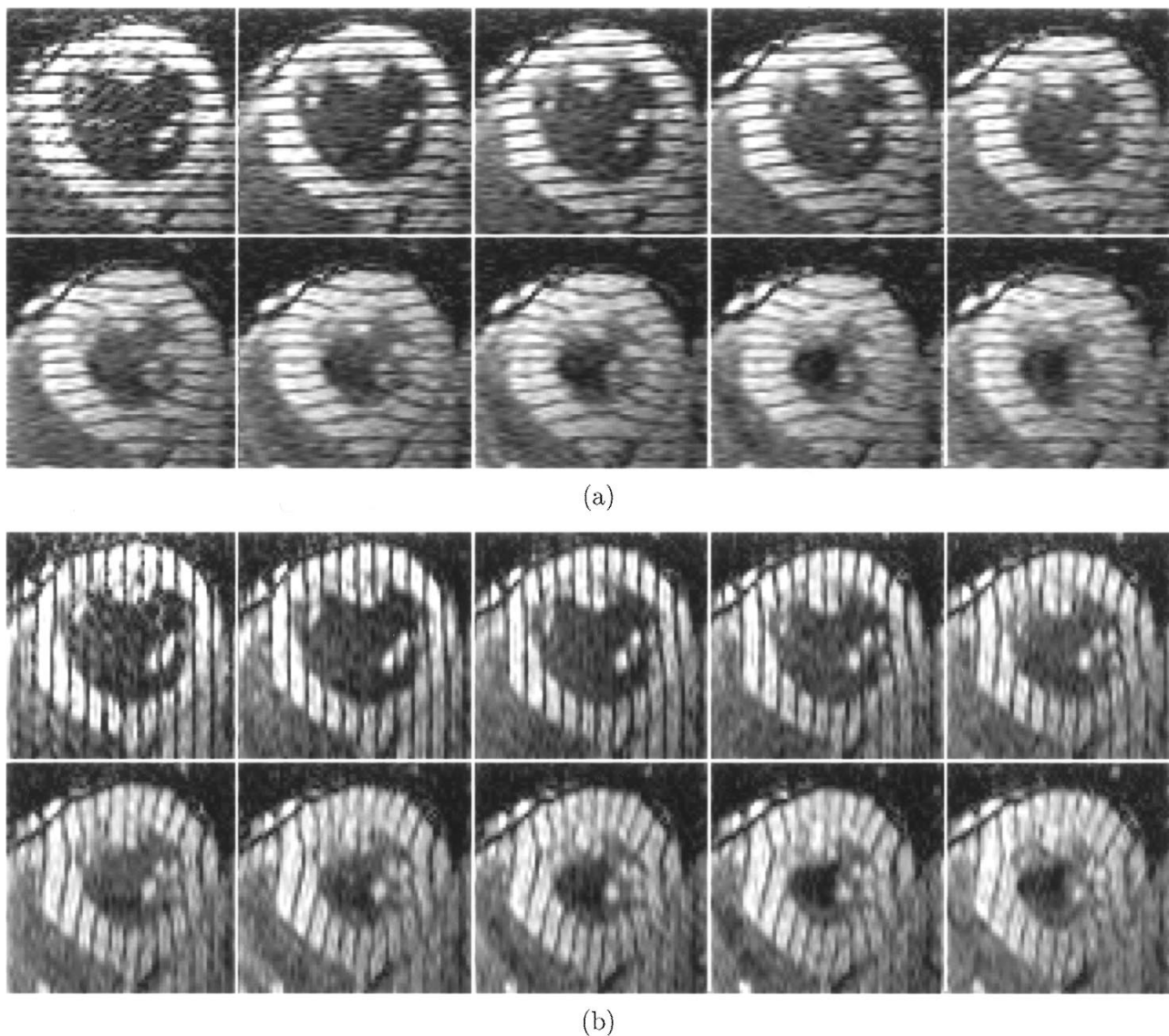
Fig. 6.   A planar tagged image sequence with (a) horizontal and (b) vertical tags showing the short-axis of the LV in systole.

of interest. A very important observation in Fig. 9 is the agreement between the synthesized tag lines and the original tags of the image, giving strong evidence that HARP images contain the same motion information as the original images. In Fig. 9(a), a single HARP image was generated from the spectral peak corresponding to the first harmonic of the underlying image. Then the HARP angle isocontour value a was set to π so that the generated lines coincided with the tag lines in the image. The lines generated in this fashion appear to very accurately track the tag lines in the image. In Fig. 9(b), two HARP images were used, one at $45°$ and the other at $135°$. For each HARP image, the isocontour angle a was manually adjusted until the generated lines appeared to coincide with the visible tag lines within the image.

The final example, shown in Fig. 9(c), demonstrates how two isocontour values can be used to generate synthetic tag lines that are closer together than the tag lines appearing in the image and that these lines do not have to coincide with those in the image. This particular image data is from a canine heart abnormally activated by a pacing lead placed at the base of the free LV wall

(approximately the one o'clock position) [48]. In this relatively early systolic image, early mechanical activation near the pacing lead is seen as the tag lines bending inward toward the LV cavity. Associated prestretching is seen in the septal wall, where the tag lines bend outward toward the right ventricle (RV) cavity. This is the correct pattern, which demonstrates that HARP images can be applied to abnormal cardiac motion as well as normal motion.

2) Measuring Small Motion: Using (18), we computed the apparent 2-D displacement field $\mathbf{u}_2$ given the horizontal and vertical tagged images at the second time frame in the image sequences (shown in Fig. 6). The resulting computed displacement field, scaled and decimated by a factor of two, is shown in Fig. 10. Here, the magnitude image was also used to create a simple threshold segmentation that masks the display of displacement vectors to those nominally in the myocardium.

Several observations can be made from Fig. 10. First, the overall motion pattern appears to be very smooth or coherent.
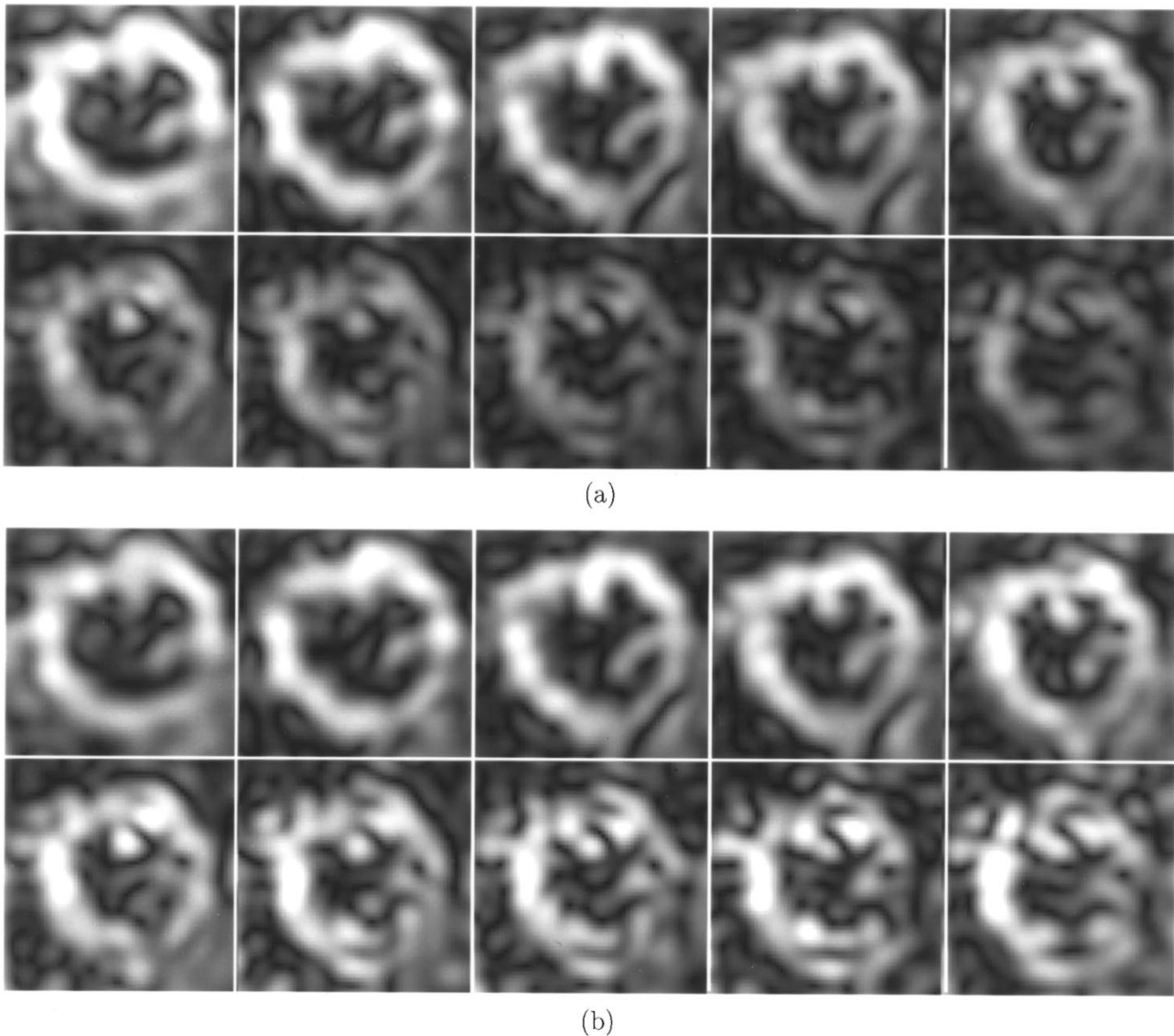
(a)

(b)

Fig. 7.   (a) Average magnitude of the complex images computed from the tagged images in Fig. 6. (b) These same images normalized to account for tag fading.

We emphasize that this is not the result of regularization or spatial smoothing. Our results are computed on a pixel-by-pixel basis. In fact, vectors outside the myocardium (not shown) are quite chaotic looking. Second, the overall pattern is one of counterclockwise rotation and careful scrutiny reveals that there is a more inward orientation of the vectors nearer the LV cavity than those farther away. This is evidence of both contraction and thickening, which we know must occur in early systole. Third, there are fairly coherent vectors appearing on the papillary muscles that extend into the LV cavity. This is initial evidence, though not conclusive by any means, that we may be able to track these muscles as well as those within the larger myocardial wall.

3) Measuring Strain: Next, we used the HARP images in Fig. 8 to compute the apparent 2-D circumferential strain during LV contraction. In order to do this, we manually specified a center point for the LV and computed unit vectors $\mathbf{e}(\mathbf{y})$ that are tangents to circles centered at this point. Equation (24) was then used to compute ϵ_2, which represents the apparent 2-D circumferential strain in this case. The quantity displayed in Fig. 11 is $\epsilon_2(\mathbf{y}, t)$ smoothed by a 7×7 averaging filter and then restricted to a simple threshold segmentation obtained from the magnitude images. The field is smoothed to compensate for noise in the gradient computation than the simple averaging filter we employed in this paper.

There are several observations we can make from Fig. 11. First, we note that this image is a midventricle LV short-axis image of a normal subject. The midventricle is typically undergoing a very simple out-of-plane motion, basically a translation and compression of the base toward the apex. Therefore, the apparent 2-D strain in a short-axis plane is a very useful diagnostic quantity. Second, overall darkening of the myocardial strain map indicates that its circumference is getting shorter, i.e., the LV is contracting. Third, there are lighter spots near the six and ten o'clock positions that indicate less shortening than in other regions. These locations happen to be the locations where the right ventricular myocardium joins the LV
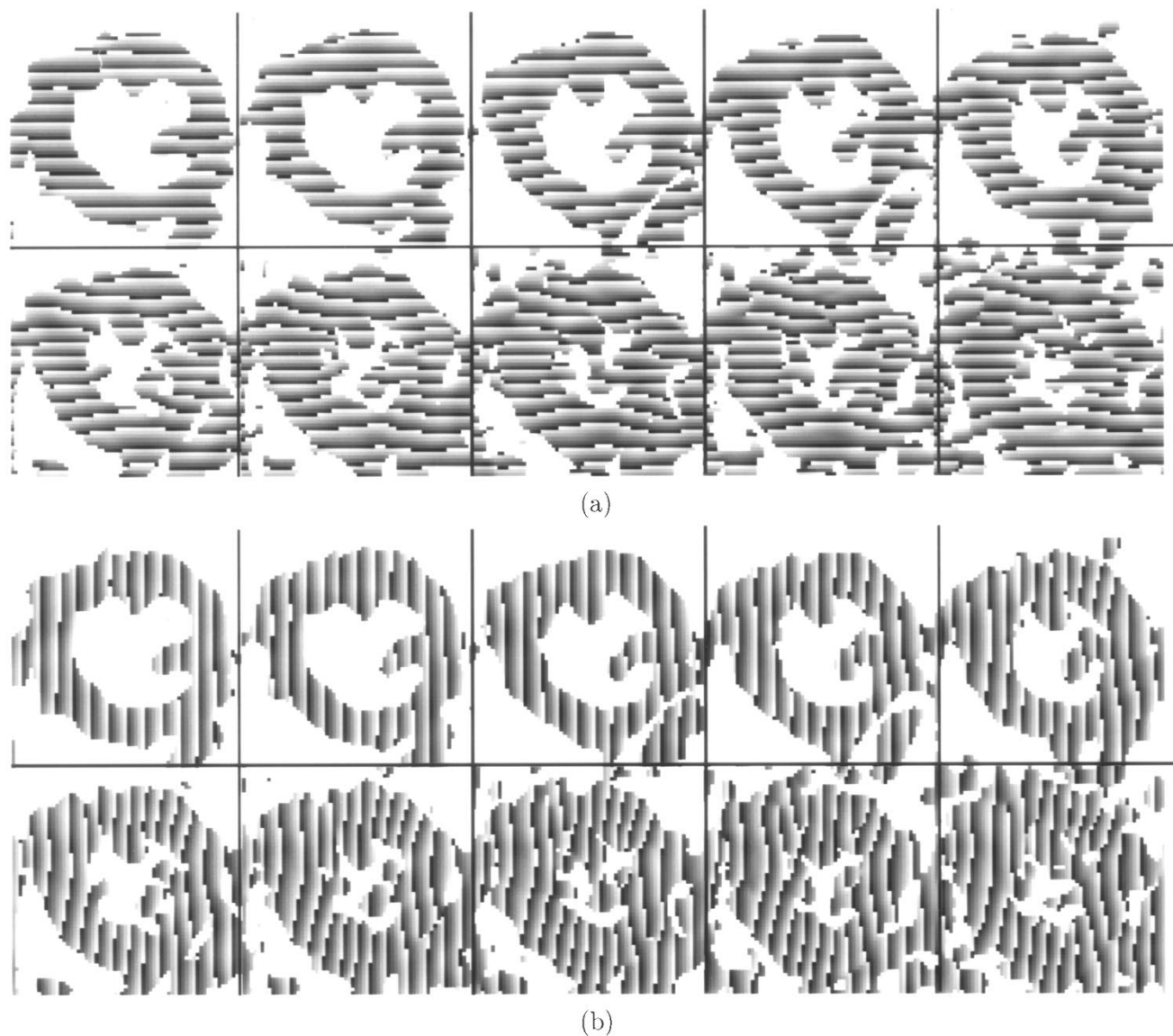
Fig. 8.   (a) Horizontal and (b) vertical angle images derived from the tagged images in Figs. 6(a) and (b), respectively.

and this behavior is expected. Finally, a slightly lighter shade throughout the septum is expected as this region normally does not undergo quite as much contraction as the free wall [8].

To demonstrate how our strain estimation procedure performs on abnormal cardiac motion, we computed the apparent 2-D circumferential strain on a full set of planar tagged image data from an abnormally paced canine heart [48]. A single image from this data set was shown in Fig. 9(c). A time sequence of computed 2-D circumferential strain estimates is shown in Fig. 12, restricted to the automatically generated myocardial segmentation obtained from the magnitude images. The time interval between the images is 19.5 ms and the tag period is 5.5 mm (for a complete description of the experiment see [48]). The third image in this sequence reveals early activation (circumferential contraction) in the one o'clock position, the location of the pacing lead, which persists for several frames. The lighter region in the septum also visible in the third frame indicates a prestretch of the myocardial fibers which persists well into the systolic phase. This indicates a significant delay of the onset of

shortening because the conduction does not travel through the normal pathways of the heart. Many of the basic conclusions presented in the 3-D analysis in [48] are evident in our results obtained in a fast completely automatic fashion.

V. DISCUSSION AND CONCLUSION

Perhaps the most important aspect of the method presented here is its computational simplicity in producing measures of motion. The basic mathematical operations here include: the inverse Fourier transform to produce a complex image; computing the HARP images; and computing the derivatives of the HARP images. These computations are fast and in few minutes the resulting strain maps are produced. For example, for the canine heart with 20 time frames, it took only three min on a 350-MHz Pentium II computer to compute the strain. Bearing in mind that the code was implemented using MATLAB, there is clearly potential for even faster computations. Also important, is the fact that the only human intervention required was the setting of the
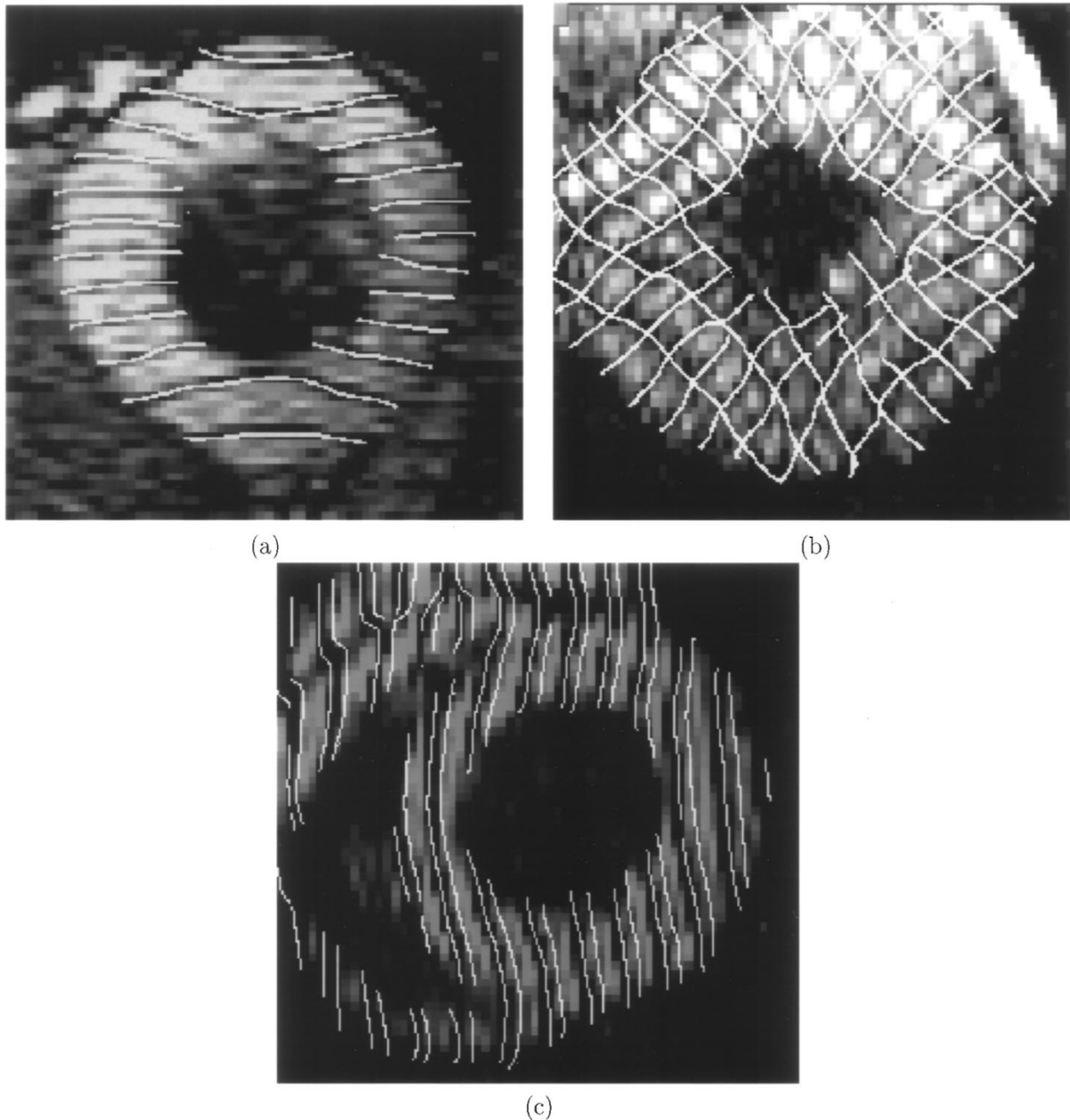
Fig. 9.   Synthesized tag lines generated from (a) the first harmonic peak of this higher-order SPAMM-tagged image, (b) two diagonal angle images of this 2-D 1-1 SPAMM-tagged image, and (c) from the first harmonic peak this higher order SPAMM-tagged image of a canine heart.

threshold level for the rough segmentation and picking the long axis position in the images to determine the radial and circumferential directions. The other settings, such as the filters size and location, were determined automatically from the tagging separation and orientation, which was set by the scanner's operator.

In the experiments presented in this paper, we have computed HARP images by extracting the spectral peaks from existing tagged MR images. Since MRI is a Fourier imaging technique, it would be more efficient to acquire only the Fourier data one needs directly from the scanner. This idea has promise for fast motion imaging using MR tagging. One approach would be to use separate 1-D SPAMM acquisitions, imaging their respec-

tive spectral peaks in separate phase-encoded sets of acquisitions. Another approach would be to use 2-D SPAMM acquisitions, orienting the read-out direction to acquire two (orthogonal) spectral peaks in one phase-encoded sets of acquisition. The increased speed of acquisition could be used to shorten breath-holds, to acquire images closer together in time, or to acquire denser 3-D image sets. On the other hand, the acquisition of separate spectral peaks might be susceptible to field inhomogeneity, so further research has to be done.

Interference from spectral peaks is a source of artifacts in our method and the dc peak is particularly problematic since its energy increases as the tags fade. Using higher frequency tags helps but, because of frequency truncation and the requirement
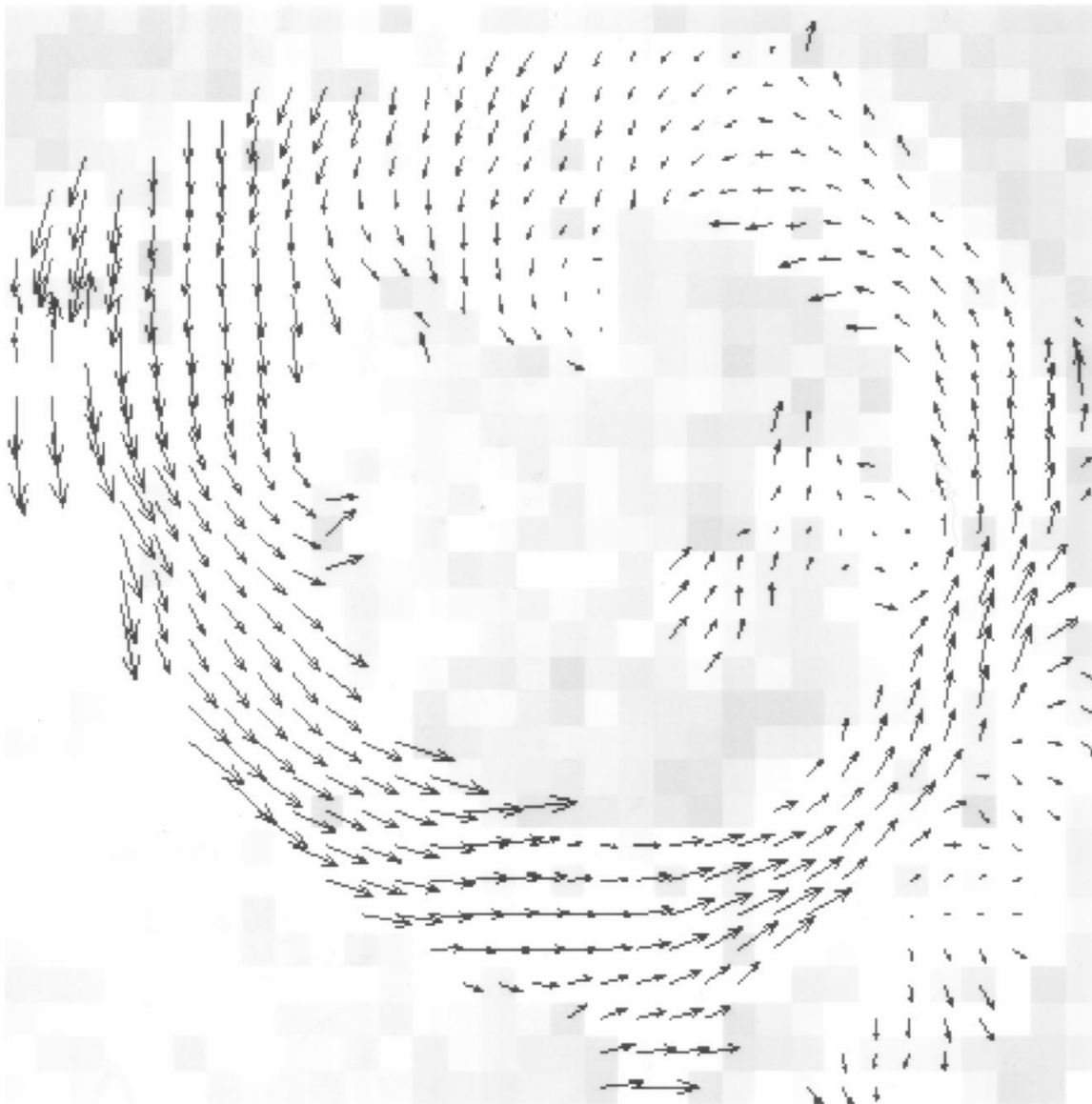
Fig. 10.   The displacement field calculated from the second pair of tagged images in the image sequence of Fig. 6.

to image larger regions in Fourier space, there is an upper bound on usable tag frequency. It turns out that direct Fourier acquisition from the scanner can help this problem as well. In particular, the use of 180° total tag tip angle will largely suppress the dc component in the early stages of acquisition. The deleterious effects of tag fading will be delayed as well because of the larger tip angle. To image later parts of the cardiac cycle (diastole), however, it would still be necessary to use midcycle tagging.

Interference from adjacent spectral peaks, including the dc peak and higher frequency peaks, can produce artifacts in the HARP methods. One example of an artifact is the blotchy or pinwheel effect seen in HARP strain maps. Another example is the branching and truncations of the HARP images within the myocardium, which occurs on rare occasions. Direct Fourier acquisition with 180° tip angles should help this problem somewhat because it suppresses the dc lobe. The use of 1-1 SPAMM should help because there will be no higher order spectral peaks with which to interfere. Also,

in 2-D 1-1 SPAMM, the 180° total tip-angle protocol also suppresses the cross terms, leaving essentially a four-peak pattern. Furthermore, the cross term peaks do not reappear as the tags fade, as does the dc peak. This bodes well for the very fast acquisition of two peaks at once, using 2-D 1-1 SPAMM. Further suppression of noise in strain computation may require a more sophisticated regularization approaches.

Because our emphasis has been on reducing image acquisition times, our approach describes the use of just two spectral peaks in Fourier space. The data we actually used in our experiments, however, had more peaks available in the data and these could have been exploited as well. For example, using the eight spectral peaks (not counting the dc peaks) available in the study of Fig. 6 might have led to improved results. Since acquiring more data in the read-out direction has virtually no extra cost associated with it, it may be beneficial to extend our methods to include linearly dependent $\mathbf{w}_k$ vectors. This would require least
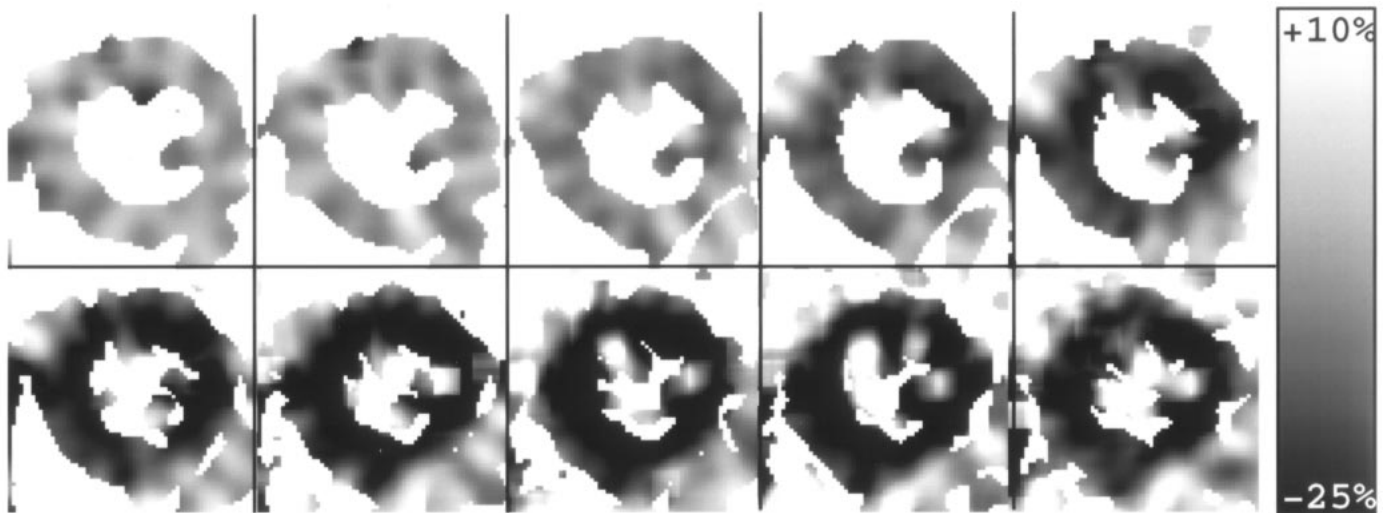
Fig. 11. The estimated circumferential strain from the complete set of the planar tagged images of the human LV shown in Fig. 6. The gray level color bar indicates the strain value, varying from the darkest level with 25% shortening to the lightest with 10% stretching.
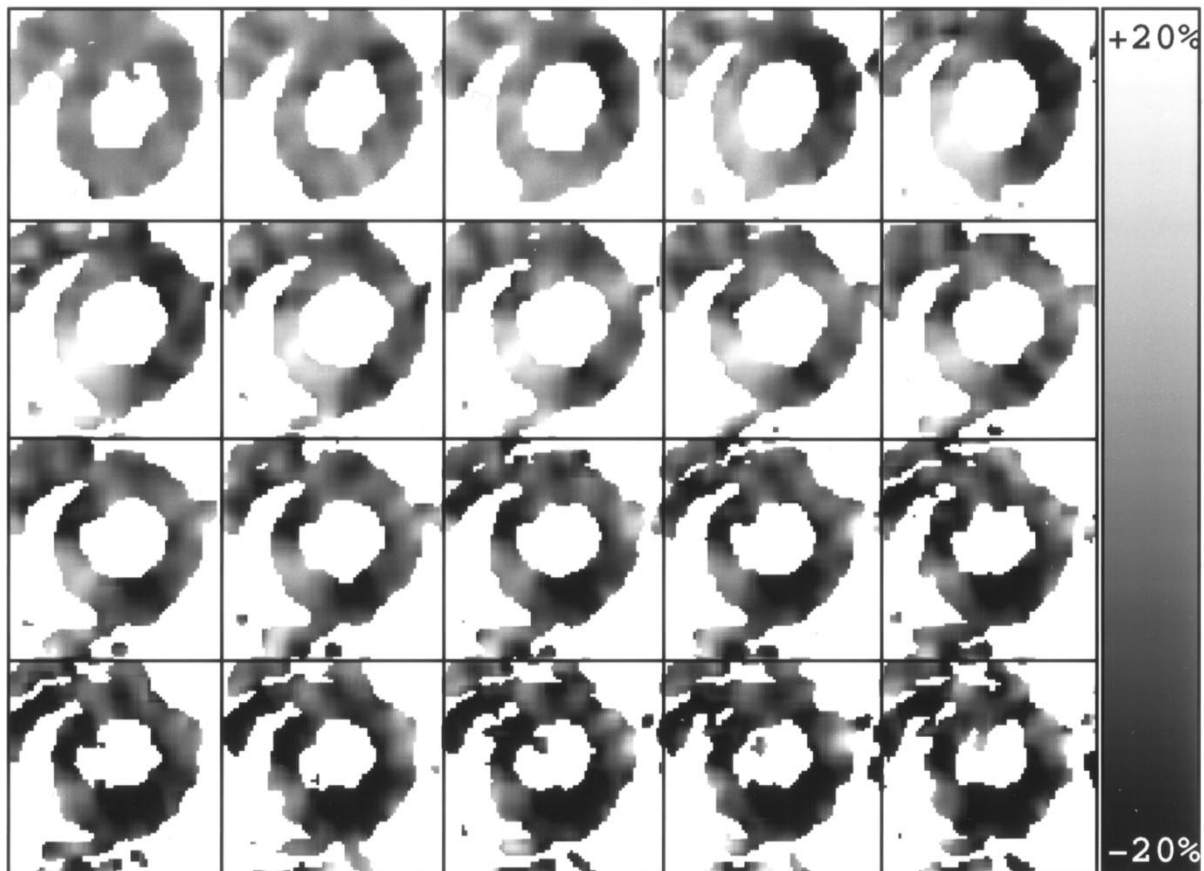

Fig. 12. The circumferential strain in a short-axis image of a paced canine LV. The gray level color bar indicates the strain value, varying from the darkest level with 20% shortening to the lightest with 20% stretching.

squares methods and would presumably lead to more accurate results (cf. [32]).

There are several ways to extend our results in this paper to 3-D. One approach is to use our synthetic tag lines in any currently existing tag line analysis methods based on orthogonal image acquisitions [15]–[17]. There should be an immediate advantage coming from the denser tag lines we can generate, although the approach would still be limited by the density of image planes. Another approach is to consider tag directions $\mathbf{w}_k$ not oriented in the image plane [40]. In this case, (11) becomes

the starting point for extending our methods to 3-D. It turns out that it is possible to reconstruct 3-D displacement vectors and the full 3-D strain tensor given adequate 3-D image data. We are actively exploring this in our current research program, and it will be the subject of a future paper.

APPENDIX

A. Proof of Small Displacement Calculations

Since the phase ϕ_k differs from the HARP angle a_k by a multiple of 2π, it follows that

$$\Delta a_k(\mathbf{y}, t) = \mathcal{W}\left[\mathbf{w}_k^T \mathbf{x}(\mathbf{y}) - \phi_k(\mathbf{y}, t)\right].$$

This can be further simplified using (8) and (11), leading to

$$\Delta a_k(\mathbf{y}, t) = \mathcal{W}\left[\mathbf{w}_k^T \mathbf{u}(\mathbf{x}(\mathbf{y}), t)\right].$$

Now if $|\mathbf{w}_k^T \mathbf{u}| < \pi$, then no wrapping will occur and

$$\Delta a_k(\mathbf{y}, t) = \mathbf{w}_k^T \mathbf{u}(\mathbf{x}(\mathbf{y}), t), \quad \text{if } |\mathbf{w}_k^T \mathbf{u}| < \pi. \tag{30}$$

From (30) we get $\Delta a_k(\mathbf{y}, t) = \mathbf{w}_k^T H \mathbf{u}_2(\mathbf{y}, t)$ and (18) follows by simple rearrangement.

B. Proof of Strain Calculations

Since the phases ϕ_k and ϕ_l are the same for $\mathbf{y}$ and $\mathbf{q}$, we can use (11) and the fact that $\mathbf{p}(\mathbf{x}, 0) = \mathbf{x}$ to show that

$$\phi_i(\mathbf{y}, t) = \mathbf{w}_i^T(H\mathbf{q} + \mathbf{x}_0)$$

for $i = k, l$. Defining $\phi = [\phi_k \ \phi_l]^T$ and rearranging yields

$$\phi(\mathbf{y}, t) = W^T H \mathbf{q} + W^T \mathbf{x}_0 \tag{31}$$

which can be solved for $\mathbf{q}$, yielding

$$\mathbf{q}(\mathbf{y}, t) = (W^T H)^{-1}[\phi(\mathbf{y}, t) - W^T \mathbf{x}_0]. \tag{32}$$

Taking the gradient of (32) yields (20).

ACKNOWLEDGMENT

The authors are grateful to M. Guttman, B. Kerwin, and S. Gupta for their comments and suggestions.

REFERENCES

[1] A. A. Young and L. Axel, "Three-dimensional motion and deformation of the heart wall: Estimation with spatial modulation of magnetization—A model-based approach," *Radiology*, vol. 185, pp. 241–247, 1992.

[2] E. R. McVeigh and E. A. Zerhouni, "Noninvasive measurements of transmural gradients in myocardial strain with MR imaging," *Radiology*, vol. 180, no. 3, pp. 677–683, 1991.

[3] C. Moore, W. O'Dell, E. McVeigh, and E. Zerhouni, "Calculation of three-dimensional left ventricular strains from biplanar tagged MR images," *J. Magn. Res. Imag.*, vol. 2, no. 2, pp. 165–175, Mar./Apr. 1992.

[4] C. M. Kramer, W. J. Rogers, G. Geskin, T. P. Power, T. M. Theobald, Y.-L. Hu, and N. Reichek, "Usefulness of magnetic resonance imaging early after acute myocardial infarction," *Amer. J. Cardiology*, vol. 80, pp. 690–695, Sept. 1997.

[5] E. Atalar and E. R. McVeigh, "Optimization of tag thickness for measuring position with magnetic resonance imaging," *IEEE Trans. Med. Imag.*, vol. 13, pp. 152–160, 1994.

[6] L. Axel and L. Dougherty, "Heart wall motion: Improved method of spatial modulation of magnetization for MR imaging," *Radiology*, vol. 172, no. 1, pp. 349–350, 1989.

[7] L. Axel and L. Dougherty, "MR imaging of motion with spatial modulation of magnetization," *Radiology*, vol. 171, pp. 841–845, 1989.

[8] E. McVeigh, "MRI of myocardial function: Motion tracking techniques," *Magn. Res. Med.*, vol. 14, no. 2, pp. 137–150, 1997.

[9] S. E. Fischer, G. C. McKinnon, M. B. Scheidegger, W. Prins, D. Meier, and P. Boesiger, "True myocardial motion tracking," *Magn. Res. Med.*, vol. 31, pp. 401–413, 1994.

[10] M. Doyle, E. G. Walsh, R. E. Foster, and G. M. Pohost, "Common k-space acquisition: A method to improve myocardial grid-tag contrast," *Magn. Res. Med.*, vol. 37, pp. 754–763, 1997.

[11] S. Zhang, M. Douglas, L. Yaroslavsky, R. Summers, V. Dilsizen, L. Fananapazir, and S. Bacharach, "A Fourier based algorithm for tracking spamm tags in gated magnetic resonance cardiac images," *Med. Phys.*, vol. 23, no. 8, pp. 1359–1369, Aug. 1996.

[12] J.-R. Liao, J. M. Pauly, T. J. Brosnan, and N. J. Pelc, "Reduction of motion artifacts in cine MRI using variable-density spiral trajectory," *Magn. Res. Med.*, vol. 37, pp. 569–575, 1997.

[13] M. A. Guttman, J. L. Prince, and E. R. McVeigh, "Tag and contour detection in tagged MR images of the left ventricle," *IEEE Trans. Med. Imag.*, vol. 13, pp. 74–88, 1994.

[14] S. Kumar and D. Goldgof, "Automatic tracking of SPAMM grid and the estimation of deformation parameters from cardiac MR images," *IEEE Trans. Med. Imag.*, Mar. 1993.

[15] W. G. O'Dell, C. C. Moore, W. C. Hunter, E. A. Zerhouni, and E. R. McVeigh, "Three-dimensional myocardial deformations: Calculations with displacement field fitting of tagged MR images," *Radiology*, vol. 195, pp. 829–835, 1995.

[16] T. S. Denney and J. L. Prince, "Reconstruction of 3-D left ventricular motion from planar tagged cardiac MR images: An estimation theoretic approach," *IEEE Trans. Med. Imag.*, vol. 14, pp. 625–635, 1995.

[17] P. Radeva, A. Amini, J. Huang, and E. Marti, "Deformable B-solids and implicit snakes for localization and tracking of SPAMM MRI-data," in *Proc. of MMBIA*, 1996, pp. 192–201.

[18] T. S. Denney, "Identification of myocardial tags in tagged MR images without prior knowledge of myocardial contours," *Proc. Inform. Processing Med. Imag.*, pp. 327–340, 1997.

[19] J. L. Prince and E. R. McVeigh, "Motion estimation from tagged MR image sequences," *IEEE Trans. Med. Imag.*, vol. 11, pp. 238–249, June 1992.

[20] S. N. Gupta and J. L. Prince, "On variable brightness optical flow for tagged MRI,", Tech. Rep. 95-13, JHU/ECE, 1995.

[21] S. N. Gupta, J. L. Prince, and S. Androutsellis-Theotokis, "Bandpass optical flow for tagged MR imaging," in *Proc. IEEE Int. Conf. Image Processing*, Santa Barbara, CA, 1997.

[22] N. J. Pelc, R. J. Herfkens, A. Shimakawa, and D. R. Enzmann, "Phase contrast cine magnetic resonance imaging," *Magn. Res. Quarterly*, vol. 7, no. 4, pp. 229–254, 1991.

[23] N. J. Pelc, M. Drangova, L. R. Pelc, Y. Zhu, D. C. Noll, B. S. Bowman, and R. J. Herfkens, "Tracking of cyclic motion with phase-contrast cine MR velocity data," *J. Magn. Res. Imag.*, vol. 5, pp. 339–345, 1995.

[24] R. T. Constable, K. M. Rath, A. J. Sinusas, and J. C. Gore, "Development and evaluation of tracking algorithms for cardiac wall motion analysis using phase velocity MR imaging," *Magn. Res. Med.*, vol. 32, pp. 33–42, 1994.

[25] F. G. Meyer, R. T. Constable, A. J. Sinusas, and J. S. Duncan, "Tracking myocardial deformation using phase contrast MR velocity fields: A stochastic approach," *IEEE Trans. Med. Imag.*, vol. 15, pp. 453–465, 1996.

[26] V. J. Wedeen, "Magnetic resonance imaging of myocardial kinematics. Technique to detect, localize and quantify the strain rates of the active human myocardium," *Magn. Res. Med.*, vol. 27, pp. 52–67, 1992.

[27] M. D. Robson and R. T. Constable, "Three-dimensional strain-rate imaging," *Magn. Res. Med.*, vol. 36, no. 4, pp. 537–546, 1996.

[28] W. H. Perman, L. L. Creswell, S. G. Wyers, M. J. Moulton, and M. K. Pasque, "Hybrid DANTE and phase-contrast imaging technique for measurement of three-dimensional myocardial wall motion," *J. Magn. Res. Imag.*, vol. 5, pp. 101–106, 1995.

[29] N. F. Osman, W. S. Kerwin, E. R. McVeigh, and J. L. Prince, "Cardiac motion tracking using CINE harmonic phase (HARP) magnetic resonance imaging," *Magn. Res. Med.*, vol. 42, pp. 1048–1060, 1999.

[30] L. Jacobson and H. Wechsler, "Deriation of optical flow using a spatiotemporal-frequency approach," *Comp. Vis. Graph. Image Processing*, vol. 38, pp. 29–65, 1987. phase-based optical flow.

[31] D. J. Heeger, "Optical flow using spatiotemporal filters," *Int. J. Comp. Vis.*, pp. 279–302, 1988. phase-based optical flow validation.

[32] D. J. Fleet and A. D. Jepson, "Computation of component image velocity from local phase information," *Int. J. Comp. Vis.*, vol. 5, no. 1, pp. 77–104, 1990. Measuring motion using phase-based optical flow.

[33] D. J. Fleet and A. D. Jepson, "Stability of phase information," *IEEE Trans. Pattern Anal. Machine Intell.*, vol. 15, pp. 1253–1268, Dec. 1993.

[34] T. J. Burns, S. K. Rogers, D. W. Ruck, and M. E. Oxley, "Discrete, spatiotemporal, wavelet multiresolution analysis method for computing optical flow," *Opt. Eng.* , vol. 33, no. 7, pp. 2236–2247, July 1994.

[35] J. L. Barron, D. J. Fleet, and S. S. Beauchemin, "Performance of optical flow techniques," *Int. J. Comp. Vis.*, vol. 12, no. 1, pp. 43–77, July 1994.

[36] B. Jahne, *Spatio-Temporal Image Processing. Theory and Scientific Applications*.   Berlin, Germany: Springer-Verlag, 1993.

[37] D. J. Fleet and A. D. Jepson, "Computation of normal velocity from local phase information," in *Proceedings CVPR'89 IEEE Computer Society Conference on Computer Vision and Pattern Recognition*.   Washington, DC: Computer Society, 1989.

[38] E. A. Zerhouni, D. M. Parish, W. J. Rogers, A. Yang, and E. P. Shapiro, "Human heart: Tagging with MR imaging—A method for noninvasive assessment of myocardial motion," *Radiology*, vol. 169, no. 1, pp. 59–63, 1988.

[39] M. Shinnar and J. S. Leigh, "Inversion of the bloch equation," *J. Chem. Phys.*, vol. 98, no. 8, pp. 6121–6128, Apr. 1993.

[40] L. Axel and L. Dougherty, "System and method for magnetic resonance imaging of 3-dimensional heart wall motion with spatial modulation of magnetization," 1990. U.S. Patent 5111820.

[41] N. F. Osman and J. L. Prince, "Direct calculation of 2D components of myocardial strain using sinusoidal MR tagging," in *Proc. SPIE Medical Imaging Conf.*, San Diego, CA, Feb. 1998.

[42] T. D. Nguyen, S. J. Reeves, and T. S. Denney Jr., "New magnetic resonance tagging technique for directly measuring the strain tensor of the in vivo human heart," in *Proc. IEEE Conf. Image Processing*, Chicago, IL, Oct. 4–8, 1998.

[43] R. M. Goldstein, H. A. Zebker, and C. L. Werner, "Satellite radar interferometry: Two-dimensional phase unwrapping," *Radio Sci.*, vol. 23, no. 4, pp. 713–720, 1988.

[44] H. Takajo and T. Takahashi, "Least-squares phase estimation from the phase difference," *J. Opt. Soc. Amer. A.*, vol. 5, no. 3, pp. 416–425, 1988.

[45] D. C. Ghiglia and L. A. Romero, "Direct phase estimation from phase differences using fast elliptic partial differential equation solvers," *Opt. Lett.*, vol. 14, no. 20, pp. 1107–1109, 1989.

[46] S. M.-H. Song, S. Napel, N. J. Pelc, and G. H. Glover, "Phase unwrapping of MR phase images using poisson equation," *IEEE Trans. Image Processing*, vol. 4, pp. 667–676, 1995.

[47] E. Waks, J. L. Prince, and A. S. Douglas, "Cardiac motion simulator for tagged MRI," in *Proc. Workshop Mathematical Methods in Medical Image Analysis*, San Francisco, CA, 1996, pp. 182–191.

[48] E. R. McVeigh, F. W. Prinzen, B. T. Wyman, J. E. Tsitlik, H. R. Halperin, and W. C. Hunter, "Imaging asynchronous mechanical activation of paced heart with tagged MRI," *Magn. Res. Med.*, vol. 39, pp. 507–513, 1998.